Compact static infrared broadband snapshot imaging spectrometer

Qinghua Yang (杨庆华)

School of Physics and Optoelectronic Engineering, Xidian University, Xi'an 710071, China

**Corresponding author: yangqh666@163.com*

Received September 2, 2013; accepted January 22, 2014; posted online February 28, 2014

A compact static infrared broadband snapshot imaging spectrometer (IBSIS) is presented. It consists of a telescope, three prisms, a focusing lens, and a detector. The first prism disperses sharply in the near-infrared (NIR) range along the vertical direction, and it is relatively non-dispersive in the mid-wave infrared (MWIR) range. The second prism is substantially more dispersive in the MWIR range than in the NIR range along the horizontal direction. The beam deviation caused by the first and second prisms can be controlled by the third prism. The IBSIS yields a two-dimensional dispersion pattern (TDP). The formulas and numerical simulation of the TDP are presented. The methods of target location calculation and spectral signature extraction are described. The IBSIS can locate multiple targets using only one frame of data, which allows for real-time detection and measurement of the energetic targets.

OCIS codes: 120.6200, 300.6190, 120.4640, 230.5480.

doi: 10.3788/COL201412.031201.

The multiplexing methods in spectral imaging include temporal multiplexing, multiplexing at the image plane, multiplexing at an entrance pupil, and multiplexing by tomographic projection.

Temporal multiplexing is commonly used to acquire image data. However, it introduces artifacts when the target is not static. These sensors include scanned slit, tunable filter, and Fourier transform spectrometers[1−34]. Traditional dispersive imaging spectrometers collect spectral image data by some forms of scanning, such as "push-broom" scanning or "whisk-broom" scanning, however, the target motion causes spatial artifacts. Fourier transform imaging spectrometers require scanning of the optical path difference between the two arms of an interferometer, but the target motion results in spectral-signature errors.

Multiplexing at the image plane is the most widely implemented spectral imaging techniques. The image-plane multiplexing instruments are embodied in nearly all commercial digital cameras and portable cameras. In these devices, pigments or dyes are lithographically placed on individual pixels on the focal plane array typically in a Bayer pattern, which may lead to aliasing problems.

Multiplexing at an entrance pupil frequently involves an arrangement of multiple parallel cameras wherein in each camera is filtered to a specific spectral band. However, this technique cannot achieve a large number of spectral samples because of the large number of required apertures.

Multiplexing by tomographic projection includes the computed-tomography imaging spectrometer (CTIS) based on a diffraction grating[35]. The CTIS operates in the visible spectrum (430−710 nm). The sensor proposed by Mooney *et al.*, based on a rotating direct-vision prism[36−41], disperses the spectra to form only a straight-line-shaped dispersion pattern at a time. It needs at least two frames of data to locate the target, therefore, it cannot locate energetic target in real time. Furthermore, the usefulness of the data obtained in two frames is substantially diminished when a target rapidly moves across the field of view and rapidly changes in time, such that its spectral signature differs between the first and second frames.

The energetic targets (e.g., the flash from an explosion, the missile plume, or the plume of a rocket) usually have two important features: rapidly evolve in time and strongly radiate a broadband spectrum that typically covers the visible, near infrared (NIR), short-wave infrared, and mid-wave infrared (MWIR) ranges. Therefore, simultaneous and rapid sampling of the target spectra is very important. Furthermore, the location of the target may be unknown. Thus, traditional spectral imaging techniques do not have enough time to scan.

The instrument in Ref. [42], based on a two-prism system, creates a chevron dispersion pattern. However, this system involving two prismatic dispersion elements results in angular deviation of the optical axis and increases the anamorphic magnification introduced by the prisms. The instrument in Ref. [43], yielding an L-shaped dispersion pattern, can detect and locate the energetic targets in real time. But it is still bulky and too complex in structure. Moreover, it is difficult in installation and calibration. The instrument in Ref. [44] is suitable for detecting and measuring the energetic targets in real time. However, the use and arrangement of the four prisms will decrease the transmission, increase the volume of the optical system, and make the optical system complex in

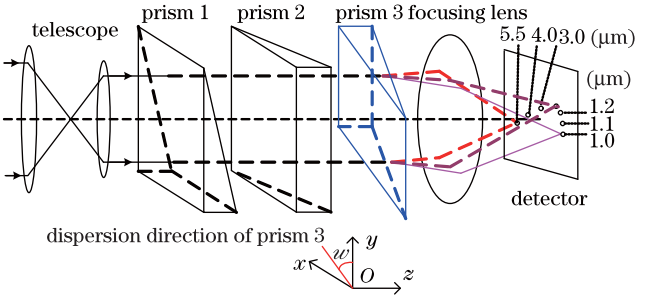

Fig. 1. Optical layout of the IBSIS.

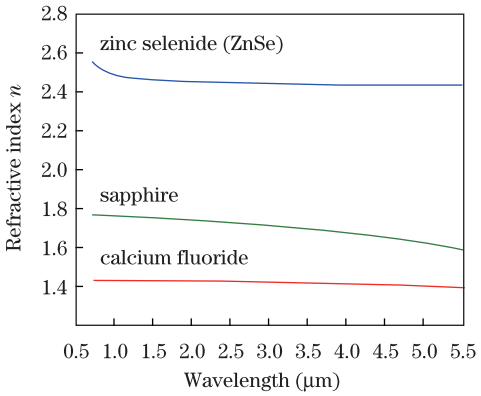

Fig. 2. Dispersion curves for ZnSe, sapphire, and CaF_2.

structure. In addition, the methods for target location estimation and spectral signature extraction are not described in Refs. [43,44].

This letter presents a compact static infrared broadband snapshot imaging spectrometer (IBSIS) with a broad spectral range from 1.0 to 5.5 μm. It is suitable for detecting and measuring the energetic targets in real time. Figure 1 shows the optical layout of the IBSIS, which includes a telescope, three prisms (prisms 1, 2, and 3), a focusing lens, and a detector. The detector is situated in the focal plane of the focusing lens. The first prism (prism 1) disperses sharply in the NIR range along the vertical direction (i.e., y-axis direction), and it is relatively non-dispersive in the MWIR range (i.e., 3.0−5.5 μm). The second prism (prism 2) is substantially more dispersive in the MWIR range than in the NIR range along the horizontal direction (i.e., x-axis direction). The third prism (prism 3) controls the beam deviation introduced by the first and second prisms. The angle between the dispersion directions of prism 3 and prism 1 is ω.

The rays emitted from a target are collected and transformed into the parallel beam by the telescope. When the parallel beam passes through the three prisms, the prism 1 will sharply disperse the wavelengths in the NIR range along the vertical direction, whereas the prism 2 will mainly disperse the wavelengths in the MWIR range along the horizontal direction. Then the focusing lens will map these dispersed wavelengths onto the detector to form a two-dimensional dispersion pattern (TDP). Each TDP will be a snapshot of the target spectra.

Due to the excellent performance in the wavelength range from 1.0 to 5.5 μm, the InSb detector is a good candidate for the IBSIS.

An advantageous material for prism 1 is ZnSe because it is sharply dispersive in the NIR range and relatively non-dispersive in the MWIR range. Sapphire is an advantageous material for prism 2 because sapphire is substantially more dispersive in the MWIR range than in the NIR range. CaF_2 is a suitable material for prism 3 because its refractive index is relatively constant over the wavelength range of 1.0−5.5 μm. The dispersion curves for ZnSe, sapphire, and CaF_2 are depicted in Fig. 2, respectively.

For convenience, suppose that α is the vertex angle of prism 1, β is the vertex angle of prism 2, and γ is the vertex angle of prism 3; $n_1(\lambda_i)$ is the refractive index of prism 1 for wavelength λ_i, $n_2(\lambda_i)$ is the refractive index of prism 2 for wavelength λ_i, and $n_3(\lambda_i)$ is the refractive index of prism 3 for wavelength λ_i; f is the focal length of the focusing lens; ϕ and φ are the angles between the emergent ray from the telescope and the optical axis in the meridian plane and sagittal plane, respectively.

The y-axis coordinate of the dispersed-wavelength imaging position can be expressed as

$$y(\lambda_i) = f\frac{\psi - \cos\omega\tan\gamma\sqrt{1-\psi^2}}{\psi\cos\omega\tan\gamma + \sqrt{1-\psi^2}}, \tag{1}$$

$$\psi = n_3(\lambda_i)\left(\frac{\cos\omega\sin\gamma\sqrt{1-\psi_1^2} - \psi_1\cos\gamma}{\sqrt{\cos^2\gamma + \cos^2\omega\sin^2\gamma}}\right), \tag{2}$$

$$\psi_1 = \frac{\psi_2\cos\alpha - \sin\alpha\sqrt{1-\psi_2^2}}{n_3(\lambda_i)}, \tag{3}$$

$$\psi_2 = \sin\alpha\sqrt{n_1^2(\lambda_i) - \sin^2\phi} - \cos\alpha\sin\phi. \tag{4}$$

The x-axis coordinate of the dispersed-wavelength imaging position can be expressed as

$$x(\lambda_i) = f\frac{\sin\omega\tan\gamma\sqrt{1-k^2} - k}{\sqrt{1-k^2} + k\sin\omega\tan\gamma}, \tag{5}$$

$$k = n_3(\lambda_i)\left(\frac{\sin\omega\sin\gamma\sqrt{1-k_1^2} - k_1\cos\gamma}{\sqrt{\cos^2\gamma + \sin^2\omega\sin^2\gamma}}\right), \tag{6}$$

$$k_1 = \frac{k_2\cos\beta - \sin\beta\sqrt{1-k_2^2}}{n_3(\lambda_i)}, \tag{7}$$

$$k_2 = \sin\beta\sqrt{n_2^2(\lambda_i) - \sin^2\varphi} + \cos\beta\sin\varphi. \tag{8}$$

When the IBSIS has none of the three prisms, the imaging location of a target is called the non-dispersed imaging location (NDIL). Therefore, each NDIL is corresponding to one target location. The y-axis and x-axis coordinates of the NDIL can be, respectively, written as[43,44]

$$y_0 = f\tan\phi, \tag{9}$$

$$x_0 = f\tan\varphi. \tag{10}$$

According to Eqs. (1)−(8), the x-axis and y-axis coordinates of the dispersed-wavelength imaging positions are shown in Fig. 3.

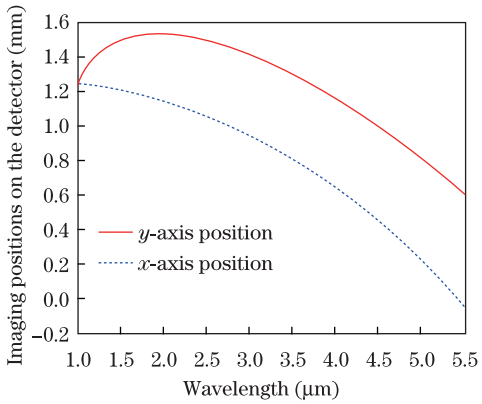

Fig. 3. Dispersed-wavelength imaging positions upon the detector in x-axis and y-axis, respectively (α=π/17.4, β=π/14, γ=π/4.6, ω=π/6, f=50 mm, ϕ=φ=π/180).

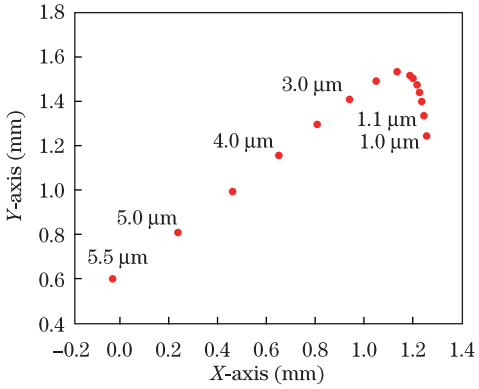

Fig. 4. TDP (α=π/17.4, β=π/14, γ=π/4.6, ω=π/6, f=50 mm, ϕ=φ=π/180).

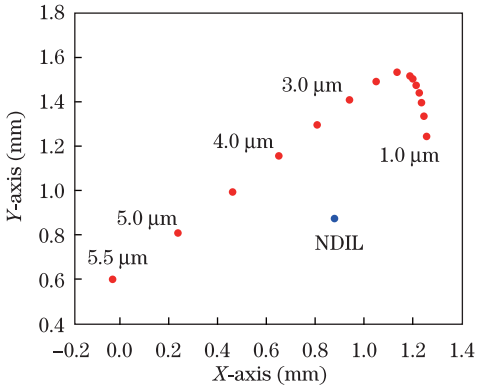

Fig. 5. Relation between the NDIL and the TDP (α=π/17.4, β=π/14, γ=π/4.6, ω=π/6, f=50 mm, ϕ=φ=π/180).

The dispersed-wavelength imaging positions on the detector will form a two-dimensional dispersion pattern (TDP) as shown in Fig. 4. For a given IBSIS (i.e., the values of α, β, γ, ω, and f are given; the materials of the three prisms are given), the shape of the TDP is fixed, and each TDP is a snapshot of the target spectra.

According to Eqs. (1)−(10), the relationship between the NDIL and the TDP is depicted in Fig. 5. For a given IBSIS, the relationship between the NDIL and the TDP is fixed. Since each NDIL is corresponding to one target location, each TDP position is corresponding to one target location.

If only one target is present in the field, only one TDP will be obtained from one frame of data. If two targets are present in the field, two TDP will be obtained from one frame of data, as shown in Fig. 6. Since each TDP position is corresponding to one target location, the IBSIS can locate two targets based only on one frame of data.

If three targets are present in the field, three TDP will be obtained from one frame of data, as shown in Fig. 7. The IBSIS can locate three targets using only one frame of data.

If four targets are present in the field, four TDP will be obtained from one frame of data, as shown in Fig. 8. The IBSIS can locate four targets using only one frame of data.

If more than four targets are present in the field, the IBSIS can also locate these targets using only one frame of data. In a word, the IBSIS can locate multiple targets using only one frame of data.

Since the shape of the TDP and the relationship between the NDIL and the TDP are fixed for a given IBSIS, we can first obtain a TDP template from an instrument calibration. Target location estimation is fitting a TDP template to the measured TDP data.

Target location estimation is a two-step process: the first step provides a coarse estimation of the location, which is accurate to the nearest pixel; the second step uses the coarse estimation to form a more accurate estimation.

The coarse location estimation can be accomplished as a convolution of the form

$$c_{m,n} = \sum_i \sum_j d_{i,j} t_{i-m,j-n}, \tag{11}$$

where $\mathbf{c}$ is the convolution image data, $\mathbf{d}$ is the measured TDP data, $\mathbf{t}$ is a TDP template obtained from an instrument calibration.

Equation (11) is often expressed in abbreviated form

$$\mathbf{c} = \mathbf{d} * *\mathbf{t}, \tag{12}$$

where $**$ indicates a two-dimensional convolution.

We first take the Fourier transform (FT) of Eq. (12)

$$\mathrm{FT}\left[\mathbf{c}\right] = \mathrm{FT}\left[\mathbf{d} * *\mathbf{t}\right] = \mathrm{FT}\left[\mathbf{d}\right] \cdot \mathrm{FT}\left[\mathbf{t}\right], \tag{13}$$

and then we take the inverse FT of equation (13)

$$c = \mathrm{FT}^{-1}\left[\mathrm{FT}\left[\mathbf{d}\right] \cdot \mathrm{FT}\left[\mathbf{t}\right]\right]. \tag{14}$$

The pixel with the greatest intensity in the resulting convolution image gives the target location to the nearest pixel.

Once the coarse location estimation is accomplished, a more accurate estimation can be obtained by calculating the intersection point of the first and second straight lines that fit to the two "arms" of the measured TDP.

Once the location of the target is known, spectral signature extraction can be accomplished as follows.

We first rearrange the measured TDP data into a vector $\mathbf{d}$ given by

$$\mathbf{d} = \mathbf{U}\mathbf{e} \tag{15}$$

where $\mathbf{U}$ is the system transfer function matrix of the optical system in the IBSIS, and $\mathbf{e}$ is the target signature.

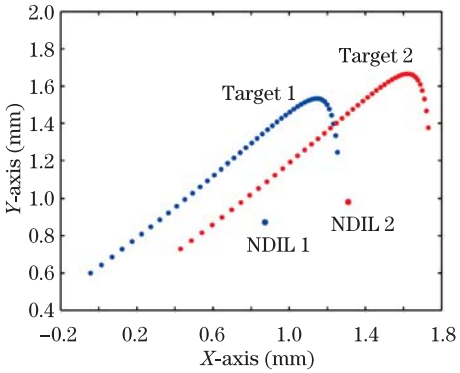

Fig. 6. Dispersion patterns for two targets (α=π/17.4, β=π/14, γ=π/4.6, ω=π/6, f=50 mm): Target 1 (ϕ_1 = φ_1 = π/180), Target 2 (ϕ_2 = π/160, φ_2=π/120).

Equation (15) can be expanded as

$$\begin{bmatrix} d_{11} \\ d_{21} \\ d_{31} \\ d_{41} \\ \vdots \\ d_{12} \\ d_{22} \\ \vdots \\ d_{n-1,n} \\ d_{n,n} \end{bmatrix} = \begin{bmatrix} u_{11}(x_1,y_1,\lambda_1)\ u_{11}(x_1,y_1,\lambda_2)\ \cdots\ u_{11}(x_2,y_2,\lambda_1)\ u_{11}(x_2,y_2,\lambda_2)\ \cdots \\ u_{21}(x_1,y_1,\lambda_1)\ u_{21}(x_1,y_1,\lambda_2)\ \cdots\ u_{21}(x_2,y_2,\lambda_1)\ u_{21}(x_2,y_2,\lambda_2)\ \cdots \\ u_{31}(x_1,y_1,\lambda_1)\ u_{31}(x_1,y_1,\lambda_2)\ \cdots\ u_{31}(x_2,y_2,\lambda_1)\ u_{31}(x_2,y_2,\lambda_2)\ \cdots \\ u_{41}(x_1,y_1,\lambda_1)\ u_{41}(x_1,y_1,\lambda_2)\ \cdots\ u_{41}(x_2,y_2,\lambda_1)\ u_{41}(x_2,y_2,\lambda_2)\ \cdots \\ \vdots\ \vdots\ \ddots\ \vdots\ \vdots\ \ddots \\ u_{12}(x_1,y_1,\lambda_1)\ u_{12}(x_1,y_1,\lambda_2)\ \cdots\ u_{12}(x_2,y_2,\lambda_1)\ u_{12}(x_2,y_2,\lambda_2)\ \cdots \\ u_{22}(x_1,y_1,\lambda_1)\ u_{22}(x_1,y_1,\lambda_2)\ \cdots\ u_{22}(x_2,y_2,\lambda_1)\ u_{22}(x_2,y_2,\lambda_2)\ \cdots \\ \vdots\ \vdots\ \ddots\ \vdots\ \vdots\ \ddots \\ u_{n-1,n}(x_1,y_1,\lambda_1)\ u_{n-1,n}(x_1,y_1,\lambda_2)\cdots u_{n-1,n}(x_2,y_2,\lambda_1)\ u_{n-1,n}(x_2,y_2,\lambda_2)\ \cdots \\ u_{n,n}(x_1,y_1,\lambda_1)\ u_{n,n}(x_1,y_1,\lambda_2)\ \cdots\ u_{n,n}(x_2,y_2,\lambda_1)\ u_{n,n}(x_2,y_2,\lambda_2)\ \cdots \end{bmatrix} \begin{bmatrix} e_1(\lambda_1) \\ e_1(\lambda_2) \\ \vdots \\ e_2(\lambda_1) \\ e_2(\lambda_2) \\ \vdots \end{bmatrix}. \tag{16}$$

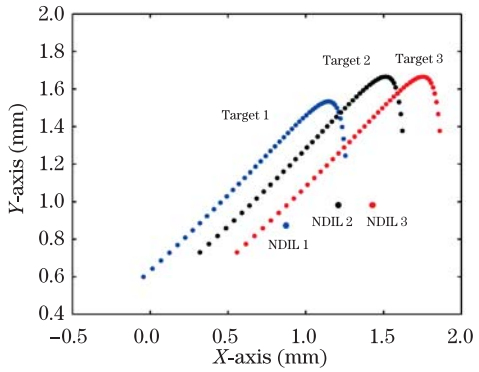

Fig. 7. Dispersion patterns for three targets (α=π/17.4, β=π/14, γ=π/4.6, ω=π/6, f=50 mm): Target 1 (ϕ_1 = φ_1 = π/180), Target 2 (ϕ_2 = π/160, φ_2=π/130), Target 3 (ϕ_3 = π/160, φ_3=π/110).

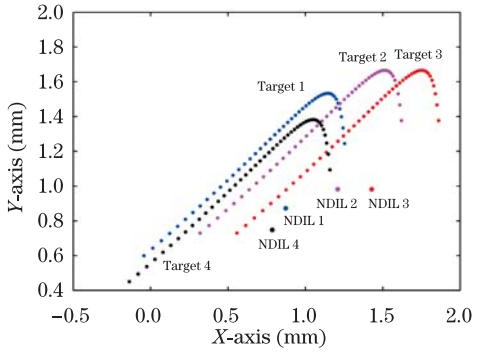

Fig. 8. Dispersion patterns for four targets (α=π/17.4, β=π/14, γ=π/4.6, ω=π/6, f=50 mm): Target 1 (ϕ_1 = φ_1 = π/180), Target 2 (ϕ_2 = π/160, φ_2=π/130), Target 3 (ϕ_3 = π/160, φ_3=π/110), Target 4 (ϕ_4 = π/210, φ_4=π/200).

The $e_k\,(\lambda_m)$ is the target signature data sampled at wavelength λ_m for target k. The $u_{i,j}\,(x_k, y_k, \lambda_m)$ is the address data, for target k, sampled at wavelength λ_m and at pixel's address of row i and column j.

The elements of matrix **U** are given by

$$u_{i,j}\,(x_k, y_k, \lambda_m) = p\,(x_i - x_k - x(\lambda_m),\ y_j - y_k - y(\lambda_m))\,, \tag{17}$$

where $p\,(x, y)$ is the spread function of the target signature; x_i and y_j are the coordinates of pixel address; $x(\lambda_m)$ and $y(\lambda_m)$ are x-axis and y-axis coordinates of the imaging position of dispersed wavelength λ_m.

We can obtain the target spectra by inverting the matrix equation

$$\mathbf{e} = \mathbf{U}^{-1}\mathbf{d}. \tag{18}$$

The IBSIS has several features as follows. First, it has a broad spectral range from 1.0 to 5.5 μm. Second, it can locate multiple targets using only one frame of data and therefore, it can locate multiple targets in real time. Third, it can obtain sub-pixel precision for locating the targets that radiate the spectra from the NIR through MWIR ranges. Fourth, it can obtain a high temporal resolution, because it is staring imaging and can realize high-speed spectral imaging. Fifth, it may have the spectral resolution of 12 nm for the NIR range and 15 nm for the MWIR range. Sixth, it is compact and has no moving parts.

Compared with the instrument in Ref. [42], the IBSIS based on a three-prism system can effectively control the beam deviation (i.e., angular deviation of the optical axis) and the anamorphic magnification introduced by the prisms.

Compared with the instrument in Ref. [43], the IBSIS based on a three-prism system will compress the volume of the optical system, decrease the weight of the optical system, make the optical system compact and simple in structure, and make the optical system easy in installation and calibration.

Compared with the instrument in Ref. [44], the IBSIS based on a three-prism system will increase the transmission, compress the volume of the optical system, decrease the weight of the optical system, and make the optical system compact.

In conclusion, a compact static IBSIS with a broad spectral range from 1.0 to 5.5 μm is presented. The IBSIS yields a TDP. I present the formulas and numerical simulation of the TDP. The methods of target location estimation and spectral signature extraction were described. The compact IBSIS without moving parts can locate multiple targets using only one frame of data. The IBSIS is well-suited to remote sensing platforms (e.g., Unmanned Aerial Vehicle and Airship) where size, weight, and power are very precious. The IBSIS is suitable for detecting, locating, and identifying energetic point targets in real time.

This work was supported by the Fundamental Research Funds for the Central Universities under Grant No. K5051305003.

References

1. A. F. H. Goetz, G. Vane, J. E. Solomon, and B. N. Rock, Science **228,** 1147 (1985).
2. H. R. Morris, C. C. Hoyt, and P. J. Treado, Appl. Spectrosc. **48,** 857 (1994).
3. M. V. R. K. Murty, J. Opt. Soc. Am. **50,** 7 (1960).
4. J. Connes and P. Connes, J. Opt. Soc. Am. **56,** 896 (1966).
5. G. Guelachvili, Appl. Opt. **16,** 2097 (1977).
6. L. Genzel and J. Kuhl, Appl. Opt. **17,** 3304 (1978).
7. W. H. Steel, *Interferometry* (Cambridge University Press, 1983).
8. J. Kauppinen and V. M. Horneman, Appl. Opt. **30,** 2575 (1991)
9. J. K. Kauppinen, I. K. Salomaa, and J. O. Partanen, Appl. Opt. **34,** 6081 (1995).
10. G. Durry and G. Guelachvili, Appl. Opt. **34,** 1971 (1995).
11. C. M. Snively, S. Katzenberger, G. Oskarsdottir, and J. Lauterbach, Opt. Lett. **24,** 1841 (1999).
12. J. Kauppinen, J. Heinonen, and I. Kauppinen, Appl. Spectrosc. Rev. **39,** 99 (2004).
13. R. K. Y. Chan, P. K. Lim, X. Wang, and M. H. Chan, Opt. Lett. **31,** 903 (2006).
14. P. R. Griffiths and J. A. de Haseth, *Fourier Transform Infrared Spectrometry* (Wiley-Interscience, 2007).
15. Q. Yang, R. Zhou, and B. Zhao, Appl. Opt. **47,** 2186 (2008).
16. Q. Yang, R. Zhou, and B. Zhao, Appl. Opt. **47,** 2486 (2008).
17. Q. Yang, R. Zhou, and B. Zhao, J. Opt. A Pure Appl. Opt. **11,** 015505 (2009).
18. Q. Yang, B. Zhao, and R. Zhou, J. Mod. Opt. **56,** 1283 (2009).
19. T. A. Al-Saeed and D. A. Khalil, Appl. Opt. **48,** 3979 (2009).
20. D. Sánchez-de-la-Llave, S. Chávez-Cerda, M. Anguiano-Morales, D. Ramirez-Martinez, M. M. Méndez-Otero, and M. D. Iturbe-Castillo, Opt. Eng. **48,** 085601 (2009).
21. Q. Yang, Appl. Opt. **49,** 4088 (2010).
22. D. F. Murphy and D. A. Flavin, Meas. Sci. Technol. **21,** 094031 (2010).
23. V. Jovanov, E. Bunte, H. Stiebig, and D. Knipp, Opt. Lett. **36,** 274 (2011).
24. C. Meneses-Fabian and U. Rivera-Ortega, Opt. Lett. **36,** 2417 (2011).
25. C. Meneses-Fabian and U. Rivera-Ortega, Opt. Laser Eng. **50,** 905 (2012).
26. C. Zhang and Y. Li, Appl. Opt. **51,** 6508 (2012).
27. Q. Yang, B. Zhao, and D. Wen, Opt. Laser Technol. **44,** 1256 (2012).
28. G. Xia, B. Qu, P. Liu, and F. Yu, Chin. Opt. Lett. **10,** 081201 (2012).
29. J. Chen, Y. Zhu, B. Liu, W. Wei, N. Wang, and J. Zhang, Chin. Opt. Lett. **11,** 053003 (2013).
30. Y. Wang, Q. Wang, D. Li, H. Deng, and C. Luo, Chin. Opt. Lett. **11,** 061101 (2013).
31. B. Yu, W. Jia, C. Zhou, H. Cao, and W. Sun, Chin. Opt. Lett. **11,** 080501 (2013).
32. T. Wang, L. Xie, H. Huang, X. Li, R. Wang, G. Yang, Y. Du, and G. Huang, Chin. Opt. Lett. **11,** 111102 (2013).
33. R. Liu, Y. Qi, X. Zheng, M. Xia, and L. Xuan, Photon. Res. **1,** 124 (2013).
34. Q. Yang, B. Zhao, and X. Zeng, Chin. Opt. Lett. **11,** 021202 (2013).
35. M. R. Descour, C. E. Volin, E. L. Dereniak, K. J. Thome, A. B. Schumacher, D. W. Wilson, and P. D. Maker, Opt. Lett. **22,** 1271 (1997).
36. J. M. Mooney, Proc. SPIE **2480,** 65 (1995).
37. J. M. Mooney, V. E. Vickers, M. An, and A. K. Brodzik, J. Opt. Soc. Am. A. **14,** 2951 (1997).
38. J. E. Murguia, T. D. Reeves, J. M. Mooney, W. S. Ewing, F. D. Shepherd, and A. K. Brodzik, Proc. SPIE **4028,** 457 (2000).
39. M. M. Weeks, J. E. Murguia, J. M. Mooney, R. J. Nelson, and W. S. Ewing, Proc. SPIE **5580,** 487 (2005).
40. F. D. Shepherd, J. M. Mooney, T. E. Reeves, D. S. Franco, J. E. Murguia, C. Wong, P. Dumont, F. Khaghani, G. Diaz, M. M. Weeks, and D. Leahy, Proc. SPIE **6660,** 66600J (2007).
41. F. D. Shepherd, J. M. Mooney, T. E. Reeves, P. Dumont, M. M. Weeks, and S. DiSalvo, Proc. SPIE **7055,** 705506 (2008)
42. R. J. Nelson, J. M. Mooney, and W. S. Ewing, Proc. SPIE **6233,** 62330M (2006).
43. Q. Yang, X. Zeng, and B. Zhao, Chin. Opt. Lett. **11,** 061202 (2013).
44. Q. Yang, Opt. Eng. **52,** 053003 (2013).